Bounds and Conditions for Compressive Digital Holography Using Wavelet Sparsifying Bases

Stijn Bettens, *Student Member, IEEE*, Colas Schretter, *Member, IEEE*, Nikos Deligiannis, *Member, IEEE*, and Peter Schelkens, *Member, IEEE*

***Abstract*—Numerous experiments have been conducted with success in the field of compressive digital holography, but the theory to determine optimal measurement conditions is lagging behind. In contrast to a prior study that expects object wavefields to be sparse in the spatial domain, we investigate how the configuration of the interferometer influences the reconstruction of wavefields that are sparse in a multiresolution orthogonal wavelet basis. In particular, we derive expressions for the coherence between the free-space wave propagation operator and the basis functions of a Shannon multiresolution representation as a function of the wavelength, the propagation distance, the image sensor's pixel pitch, and the scale of the basis functions. These expressions reveal that the coherence as a function of the Fresnel number is subject to specific scaling and translating rules as the scale of the basis functions changes. For a multiresolution orthogonal wavelet representation and digital holograms that are recorded in the near field, we deduce subsequently the optimal configuration of the interferometer and we show by means of hypothesis testing that the associated phase transition bound coincides with the weak threshold for block-sparse compressive sensing with a block length of 2, which is an optimal bound for the class of complex-valued compressive sensing problems. By means of experiments with a USAF 1951 resolution target and an angle grid, we validate our findings and demonstrate that the reconstructed object wavefields are resilient to sparsity defects and additive noise.**

***Index Terms*—Compressive sensing, digital holography, fresnel number, orthogonal wavelet transforms, coherence, phase transition diagrams.**

I. Introduction

HOLOGRAPHY is a three-dimensional interference-based imaging methodology for capturing simultaneously the amplitude and phase of complex-valued wavefields. When a coherent light source illuminates an object, we can derive from the phase of the resulting wavefield a depth map with submicron accuracy. The shape (spatial phase variation) and deformation (temporal phase variation) of small objects with limited depth are measured this way. Applications include the visualization of transparent cell cultures [1], the characterization of optical components [2], and particle image velocimetry [3].

In digital holography, we capture wavefields indirectly with a digital, lens-less camera. Planes that are positioned near the object or intersect with it are of interest because the focal depth is typically less than 1 mm [4]. We note there is always a gap between the object and the camera so that the object wave can interfere with a reference wave to form an interference pattern. The captured interferogram is sampled and digitized by the camera's image sensor and a set of one or more interferograms is processed computationally to obtain the digital hologram [5], which is the complex amplitude of the object wave at the plane that contains the image sensor. The relationship between the digital hologram and the object wavefield in a parallel plane near the object is modelled by an allpass filter as specified by scalar diffraction theory [6]. Inverse filtering the digital hologram is better known as numerical back propagation and is the standard method for reconstructing the object wavefield in a plane of interest [4].

A. Related Work

When no more than a subset of the hologram samples is acquired or multiple wavefields are superposed to form a single two-dimensional (2-D) hologram, the problem of reconstructing the object wavefield(s) is ill-posed and cannot be accomplished using inverse filtering. These inverse problems belong to the field of compressive digital holography for which the works that have been published are mainly experimental in nature. In [7], for example, a proof-of-concept is provided in order to demonstrate that a free-space wave propagation operator in combination with Hadamard patterns yields a linear measurement system with the right properties for compressive sensing (CS): a generic theory in signal processing that deals with the recovery of sparse data from an underdetermined set of linear measurements [8]–[10]. Furthermore, several works report how to infer from a single 2-D hologram the shapes and geometrical positions of multiple objects in 3-D space. The authors of [11] propose the digital tomographic compressed holography method; by guiding the object wave twice through a sample of bubbles they determine the sizes of the bubbles and track their

Manuscript received April 7, 2017; revised September 4, 2017; accepted September 23, 2017. Date of publication October 10, 2017; date of current version November 6, 2017. This work was supported in part by the European Research Council under the European Union's Seventh Framework Programme (FP7/2007–2013)/ERC Grant Agreement 617779 (INTERFERE), in part by the Research Foundation—Flanders (FWO)/Project G024715N, and in part by the VUB Strategic Research Programme M3D2. The associate editor coordinating the review of this manuscript and approving it for publication was Prof. Mathews Jacob. *(Corresponding author: Stijn Bettens.)*

The authors are with the Department of Electronics and Informatics (ETRO), Vrije Universiteit Brussel, Brussels B-1050, Belgium, and also with the IMEC, Leuven B-3001, Belgium (e-mail: sbettens@etrovub.be; cschrett@etrovub.be; ndeligia@etrovub.be; pschelke@etrovub.be).

This paper has supplementary downloadable material available at http://ieeexplore.ieee.org. The material includes MATLAB code to recreate the figures and to visualize a few expressions.

Color versions of one or more of the figures in this paper are available online at http://ieeexplore.ieee.org.

Digital Object Identifier 10.1109/TCI.2017.2761742

positions. Compressive sensing is also the keystone to recover multiple flat objects that lie in a set of equidistantly-spaced planes [12], [13] and to determine the 3-D distribution of the refractive index of transparent cells using a planar cross-sectional representation [14]. We note that the aforementioned methods expect that the objects are sparse in the spatial domain so that none of the objects is severly occluded by other ones in front, which would demand for more computationally intensive wave propagation models as those in [15].

Regarding the random undersampling of wave fields, we find applications of CDH in Single-shot phase imaging [16]–[18]. A coded aperture that occludes samples in a random fashion is placed somewhere in between the object under study and the camera. Using methods from coherent diffractive imaging, the non-occluded samples are recovered. Subsequently, CDH is applied to recover the object wave field, which can be sparse in any appropriate domain.

For an exhaustive list of papers that have emerged in the field of compressive digital holography we refer to [19].

B. Problem Statement

Insight into the proper arguments and conditions that explain the many successful experiments in compressive digital holography is missing. Only the authors of [20] describe by means of an approximative coherence study how the configuration of the interferometer influences the reconstruction of wavefields that are sparse in the spatial domain. The required amount of linear measurements to obtain perfect reconstructions with overwhelming probability is predicted by the coherence up to an unknown strictly positive constant. The bounds are thus not tight. In other words, [20] does not specify exactly how sparse the object wavefields have to be such that the reconstruction error is zero with overwhelming probability.

C. Contributions

Wavefields whose unwrapped phase profiles contain the information for inferring the shape and refractive index of the illuminated object are rather sparse in a multiresolution (orthogonal) wavelet representation than the spatial domain [21]–[23]. We consider therefore 1-D and 2-D object wavefields that are sparse in a generic multiresolution orthogonal wavelet basis. As a wave propagation model we use the propagation of the angular spectrum and we solve the (quadratically constrained) ℓ_1-minimization problem for reconstructing object wavefields from undersampled holograms. Our particular contributions are as follows:

1) For the coherence between the Shannon multiresolution representation and the angular spectrum method, we derive closed-form expressions that depend on the Fresnel number. These expressions are representative for a generic orthogonal wavelet transform.
2) We obtain scaling and shifting rules for the coherence as the scale of the basis functions halves or doubles.
3) We determine phase transition bounds for different Fresnel numbers and we show that the weak threshold for block-sparse compressive sensing with a block length of 2 (see [24]), corresponds with the bound that is associated with an optimally configured interferometer.

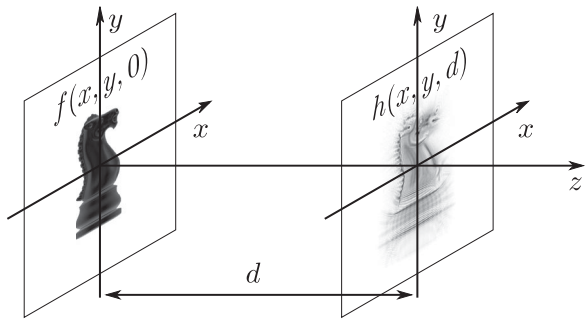

Fig. 1. Geometry of the object wavefield and the corresponding hologram with respect to a right-handed Cartesian coordinate system whose z-axis coincides with the optical axis.

D. Outline

In Section II, we describe the measurement model for compressive digital holography. In Section III, we analyse the coherence for wavefields that are sparse in a Shannon multiresolution representation with the emphasis on the relationships between different resolutions or scales, and the physical interpretation. The phase transition bounds in Section IV validate our coherence analysis. And we conclude this work in Section VI.

II. Background

A. Scalar Diffraction Theory

We consider planar wavefields over the xy-planes of a right-handed Cartesian coordinate system whose z-axis coincides with the optical axis, see Fig. 1. Let $f(x, y, z = 0) : \mathbb{R}^2 \to \mathbb{C}$ be the object wavefield and $h(x, y, z = d) : \mathbb{R}^2 \to \mathbb{C}$ the corresponding hologram (also called the image wavefield). The optical axis intersects with both wavefields at their origins, which are a distance d apart. To be specific, x and y are the arguments in the spatial domain whereas d is a parameter.

Scalar diffraction theory states that the propagation of monochromatic wavefields acts like a spatial all-pass filter [6]. In the paraxial approximation, the relationship between f and h is namely described by the equality

$$h(x, y, d) = \mathcal{F}^{-1}\left\{G_{\lambda,d}(f_x, f_y)\,\mathcal{F}\{f(x, y, 0)\}\right\}, \qquad (1)$$

where f_x and f_y are the arguments in the frequency domain, $\mathcal{F}\{.\}$ and $\mathcal{F}^{-1}\{.\}$ are respectively the 2-D unitary Fourier transform and its inverse, and

$$G_{\lambda,d}(f_x, f_y) = \exp\left[j\pi\lambda d\left(f_x^2 + f_y^2\right)\right] \qquad (2)$$

is the wave propagation filter's transfer function, which is dependent on the propagation distance d and the wavelength λ.

We sample the wavefields around the optical axis on a regular rectangular grid with N_x and N_y points in respectively the x- and y-directions. The sample periods along the x-, y-, f_x- and f_y-axes are respectively Δx, Δy, $\Delta f_x = (N_x \Delta x)^{-1}$ and $\Delta f_y = (N_y \Delta y)^{-1}$. Next, we place the samples of f and h in

lexicographical order in the vectors $\mathbf{f}$ and $\mathbf{h}$, which are both elements of $\mathbb{C}^{N_x N_y}$, so that we can write the discretization of (1) in matrix-vector notation as

$$\mathbf{h} = \mathbf{F}^{-1}\mathbf{G}_{\lambda,d}\mathbf{F}\mathbf{f} = \mathbf{\Phi}_{\lambda,d}\mathbf{f}, \tag{3}$$

where the left matrix multiplications with $\mathbf{F}$ and $\mathbf{F}^{-1}$ are equivalent to respectively the discrete Fourier transform and its inverse, and $\mathbf{G}_{\lambda,d}$ is a diagonal matrix with the samples of $G_{\lambda,d}(k\Delta f_x, \ell\Delta f_y)$ in lexicographical order on the main diagonal. As a result, the propagation of the angular spectrum is simply represented by the linear transformation $\mathbf{\Phi}_{\lambda,d}$. Furthermore, we observe in (3) that $\mathbf{G}_{\lambda,d}$ holds the eigenvalues of $\mathbf{\Phi}_{\lambda,d}$. Their moduli are all equal to 1 as a property of the complex exponential in (2). Hence, this problem is perfectly conditioned and the numerical back propagation method retrieves $\mathbf{f}$ by left multiplication of $\mathbf{h}$ with the inverse of $\mathbf{\Phi}_{\lambda,d}$.

If $\Delta x = \Delta y$ and $N_x = N_y = N$, we find that

$$G_{\lambda,d}\left(k\Delta f_x, \ell\Delta f_y\right) = \exp\left[j\pi\frac{\lambda d}{\Delta x^2}\left(\frac{k^2+\ell^2}{N}\right)\right]. \tag{4}$$

For this case, we can group the parameters λ, d and Δx in a single parameter called the Fresnel number, which is defined as

$$N_F = \frac{\Delta x^2}{\lambda d}. \tag{5}$$

We can thus parametrize the family of wave propagation filters in terms of $N_F > 0$. We use $\mathbf{\Phi}_{N_F}$ as an alias of $\mathbf{\Phi}_{\lambda,d}$ accordingly.

Concerning the wave propagation filters, we note that (3) is only valid if N_F is within certain bounds. Based on the experiments with paraboloidal reflectors in [25], we propose that $d > 100\lambda$, and the condition $N^{-1} < N_F$ has to be satisfied in order to avoid excessive aliasing as a consequence of undersampling $G_{\lambda,d}$ [26].

Hence, the Fresnel number is bounded from below and above by the inequality

$$N^{-1} < N_F < \frac{100\lambda^2}{\Delta x^2}. \tag{6}$$

B. Compressive Sensing

Let us asssume that f is band-limited and sampled at a frequency above the Nyquist rate. If the resulting sequence of samples is sparse in a certain basis or dictionary, then the compressive sensing theory states that f can be reconstructed from fewer linear measurements than what is dictated by the Shannon-Nyquist sampling theorem [27]. Let the vector of wavelet coefficients $\mathbf{x}_0 = \mathbf{\Psi}\mathbf{f}$, where $\mathbf{\Psi}$ denotes an orthogonal wavelet transform in contrast to the identity function in [20]. If $\mathbf{x}_0$ is sufficiently sparse, then we can reconstruct $\mathbf{f}$ from M linear measurements where $M \ll N^r$ for r-D wavefields [9].

In compressive digital holography, (randomly selected) hologram samples are the measurements. Let the vectors $\mathbf{y}$ and $\mathbf{T}_M\mathbf{h}$ hold respectively the measured and computed hologram samples, where $\mathbf{h}$ is defined in (3) and $\mathbf{T}_M$ is a boolean matrix that encodes the selection of the samples. We obtain an estimate of $\mathbf{x}_0$ by solving

$$\begin{aligned} &\underset{\mathbf{x}\in\mathbb{C}^N}{\text{minimize}} && \|\mathbf{x}\|_p \\ &\text{subject to} && \left\|\mathbf{y} - \mathbf{T}_M\mathbf{\Phi}_{N_F}\mathbf{\Psi}^{-1}\mathbf{x}\right\|_2 \le \epsilon, \qquad (\mathbf{P}_{p,\epsilon}) \end{aligned}$$

where $\epsilon \in \mathbb{R}^+$, $\|\cdot\|_p$ denotes the p-norm, and $\mathbf{\Psi}^{-1}$ denotes the inverse orthogonal wavelet transform.

In the presence of additive noise and sparsity defects, a non-zero ϵ bounds from above the maximum Euclidean distance between the measured and computed hologram samples. The sparsest vector of wavelet coefficients that satisfies this constraint is the solution of ($\mathrm{P}_{0,\epsilon}$). However, this is a combinatorial optimization problem and consequently intractable. The solution of ($\mathrm{P}_{1,\epsilon}$) is advocated as a substitute because 1 is the smallest value of p for which ($\mathrm{P}_{p,\epsilon}$) is a convex optimization problem. Substituting the ℓ_1 norm for the ℓ_0 pseudo-norm yields the convex relaxation of ($\mathrm{P}_{0,\epsilon}$) [28]. Let $\mathbf{x}_0$ be S-sparse and $\epsilon = 0$. For sufficiently small S, the solutions of ($\mathrm{P}_{0,0}$) and ($\mathrm{P}_{1,0}$) coincide; a property we refer to by the term '(ℓ_0, ℓ_1)-equivalence' [8], [29].

Expressions of tight bounds on the conditions that guarantee (ℓ_0, ℓ_1)-equivalence with overwhelming probability exist for compressive sensing [30]–[33] and compressive sensing with (multiple) side information [34]–[37] for the specific case of Gaussian linear measurements. Searching for similar expressions in the case of deterministic linear transformations is intractable nevertheless. We rely therefore on loose bounds that are predicted by a performance measure that is easy to compute: the coherence.

Let us define the N^r by N^r unitary measurement matrix $\mathbf{U} = \mathbf{\Phi}_{N_F}\mathbf{\Psi}^{-1}$ for r-D wavefields. The mutual coherence between $\mathbf{\Phi}_{N_F}$ and $\mathbf{\Psi}^{-1}$, or simply the coherence of $\mathbf{U}$, is defined as

$$\mu(\mathbf{U}) = \max_{k,\ell}|U_{k,\ell}| \in [1/\sqrt{N^r}, 1], \tag{7}$$

where $k, \ell \in \{1, 2, \cdots, N^r\}$ and $U_{k,\ell}$ denotes the element on the kth row and ℓth column of $\mathbf{U}$. The coherence is a good indicator, but leads to loose bounds [38]. We complement therefore the coherence study with empirical phase transition bounds in order to quantify the (ℓ_0, ℓ_1)-equivalence bound both accurately and precisely. Let the undersampling factor $\delta = M/N^r$ and the oversampling factor $\rho = S/M$. A phase transition diagram $\pi(\delta, \rho) : [0, 1]^2 \to [0, 1]$ maps the phase space pairs (δ, ρ) to the probability that an arbitrary $(\delta\rho N^r)$-sparse vector $\mathbf{x}_0$ is the unique solution of ($\mathrm{P}_{1,0}$). In this context, the phase transition bound $\rho_{0.5}(\delta)$ is defined as the solution of $\pi(\delta, \rho_{0.5}(\delta)) = 1/2$. It divides the phase space in a part where the (ℓ_0, ℓ_1)-equivalence property is not satisfied (failure) and satisfied with overwhelming probability (success).

III. Coherence Analysis

In (digital) holography, accustomed object wavefields are characterized by spectral densities that are non-increasing as the frequency increases. The Shannon wavelet transform is optimal for representing such signals [39], [40]. We formulate therefore in this section the infinite-dimensional compressive digital holography problem for object wavefields that are sparse

in a Shannon multiresolution representation. The description of these basis functions in the continuous frequency domain is suitable for deriving closed-form expressions for the coherence as a function of the Fresnel number and the scale of the basis functions. For other orthogonal wavelet transforms (over a finite domain), the specific shape of the coherence as a function of the Fresnel number alters, but the overall trends are the same as for the Shannon multiresolution representation because all of them analyze signals the same way in the time-frequency domain. We validate this statement with numerical experiments using the Battle-Lemarié, Coiflet, Daubechies, and symmlet wavelet families.

A. Infinite-Dimensional Compressive Digital Holography

Compressive sensing copes with finite-dimensional vectors like $\mathbf{f}$ and $\mathbf{h}$, whereas we consider the continuous functions f and h in the infinite-dimensional vector spaces of bounded functions:

$$\mathcal{B}_r(\mathbb{C}) = \{f : \mathbf{x} \in \mathbb{R}^r \to \mathbb{C} \mid |f(\mathbf{x})| \leq B \in \mathbb{R}^+\}$$

for r-D wavefields. We can focus on the analysis of the coherence for 1-D wavefields because the definition of the coherence in (7), the transfer function of the wave propagation filter in (2), and the basis functions of the orthogonal wavelet transform $\mathbf{\Psi}$ are all separable functions. For extending our results to 2-D wavefields, we just raise our expressions for the coherence to the second power [41].

Let $g_{\lambda,d}(x)$ be the impulse response of the wave propagation filter, which is denoted by $\mathbf{\Phi}_{N_F}$. We define the translated impulse responses $\phi_k(x) = g_{\lambda,d}(k\Delta x - x)$ and the wavelets $\psi_\ell(x)$ for $k, \ell \in \mathbb{Z}$. The rows of $\mathbf{\Phi}_{\lambda,d}$ hold translated impulse responses because $\mathbf{\Phi}_{\lambda,d}$ represents a linear space-invariant filter, and the columns of $\mathbf{\Psi}^{-1}$ hold the wavelets. We deduce from the equality $\mathbf{U} = \mathbf{\Phi}_{N_F}\mathbf{\Psi}^{-1}$ that element $\mathbf{U}_{k,\ell}$ is the inner product of the kth row of $\mathbf{\Phi}_{\lambda,d}$ and the ℓth column of $\mathbf{\Psi}^{-1}$. As the dimensions of the square measurement matrix $\mathbf{U}$ go to infinity, $\mathbf{U}$ converges to

$$\begin{array}{c} \\ \boxed{k=-1} \\ \boxed{k=0} \\ \boxed{k=1} \end{array} \begin{array}{c} \begin{array}{ccccc} & \boxed{\ell=-1} & \boxed{\ell=0} & \boxed{\ell=1} & \end{array} \\ \begin{bmatrix} \ddots & \vdots & \vdots & \vdots & \iddots \\ \cdots & \langle\phi_{-1},\psi_{-1}\rangle & \langle\phi_{-1},\psi_0\rangle & \langle\phi_{-1},\psi_1\rangle & \cdots \\ \cdots & \langle\phi_0,\psi_{-1}\rangle & \langle\phi_0,\psi_0\rangle & \langle\phi_0,\psi_1\rangle & \cdots \\ \cdots & \langle\phi_1,\psi_{-1}\rangle & \langle\phi_1,\psi_0\rangle & \langle\phi_1,\psi_1\rangle & \cdots \\ \iddots & \vdots & \vdots & \vdots & \ddots \end{bmatrix} \end{array}$$

in the weak operator topology [42], where $\langle\cdot,\cdot\rangle$ denotes the standard inner product for square-integrable functions. Hence,

$$\mathbf{U}_{k,\ell} = \int_{-\infty}^{+\infty} \psi_\ell(x) g_{\lambda,d}(k\Delta x - x)\mathrm{d}x, \tag{8}$$

and we discern that the ℓth column of $\mathbf{U}$ holds samples of the wave propagation filter's response to the ℓth wavelet. As a consequence, the maximum modulus among all continuous wavelet responses is equal to the quantity of interest; namely, the coherence $\mu(\mathbf{U})$.

B. Shannon Approximations at the Finest Scale

We divide the set of basis functions that make up the Shannon multiresolution representation into subsets that are invariant to translations by a multiple of Δx. At first, we consider the set

$$\Psi_0 = \{\psi_{0,t}(x) = \mathrm{sinc}((x - t\Delta x)/\Delta x)\}_{t\in\mathbb{Z}},$$

which is composed of the Shannon approximation functions at scale $(\Delta x)^1$. This set is characterized by translations of $\psi_{0,0}(x)$, whose unitary Fourier transform is $\Psi_{0,0}(f_x) = \Delta x\,\mathrm{rect}(\Delta x f_x)$. The rectangular function is defined as

$$\mathrm{rect}(f_x) := \begin{cases} 0 & \text{if } |f_x| > 1/2 \\ 1 & \text{if } |f_x| < 1/2, \\ 1/2 & \text{if } |f_x| = 1/2 \end{cases}$$

and $\langle\psi_{0,0}(x), \psi_{0,0}(x)\rangle = \langle\Psi_{0,0}(f_x), \Psi_{0,0}(f_x)\rangle = 1$ so the basis functions in Ψ_0 are normalized. Since the wave propagation filter is space-invariant, it is sufficient to calculate the response to $\psi_{0,0}(x)$ for determining the coherence between the wave propagation filter and the set Ψ_0. We obtain an expression for that response by drawing on Theorem 1.

Theorem 1 (based on the Corrolary in Appendix A.13 of [4]). Let β, $W \in \mathbb{R}_0^+$, where W is the half-width of a rectangular function. The inverse unitary Fourier transform of

$$\exp\left(j\pi\beta f_x^2\right)\mathrm{rect}\left(\frac{f_x}{2W}\right) \tag{9}$$

is

$$\frac{\exp\left(-j\pi\frac{x^2}{\beta}\right)}{\sqrt{2\beta}}\left(F_r(a(x)) - F_r(b(x))\right), \tag{10}$$

where $a(x) = \sqrt{2\beta}(W + x/\beta)$, $b(x) = \sqrt{2\beta}(-W + x/\beta)$, and

$$F_r(x) = \int_0^x \left(\cos\left(\frac{\pi t^2}{2}\right) + j\sin\left(\frac{\pi t^2}{2}\right)\right)\mathrm{d}t \tag{11}$$

is the Fresnel integral.

The response of the wave propagation filter to $\psi_{0,0}(x)$ is

$$y_{0,0}(x) = \mathcal{F}^{-1}\left\{\Psi_{0,0}(f_x)\,G_{\lambda,d}(f_x)\right\}. \tag{12}$$

We compare $\Psi_{0,0}(f_x)\,G_{\lambda,d}(f_x)$ with (9) and find that $\beta = \lambda d$ and $W = (2\Delta x)^{-1}$. The wavelet response $y_{0,0}(x)$ is thus a specific instantiation of (10), but we prefer to express all wavelet responses in this paper as a function of $x = \bar{x}\cdot\Delta x$ because then the expressions for the coherence become also a function of the Fresnel number. As such, we find that the expression for $y_{0,0}(\bar{x}, N_F)$ is

$$\frac{\exp\left(-j\pi N_F\bar{x}^2\right)}{\sqrt{2N_F^{-1}}}\left(F_r(a_0(\bar{x}, N_F)) - F_r(b_0(\bar{x}, N_F))\right), \tag{13}$$

where

$$a_0(\bar{x}, N_F) = \sqrt{2}\left(\bar{x}\sqrt{N_F} + \frac{1}{2\sqrt{N_F}}\right), \tag{14}$$

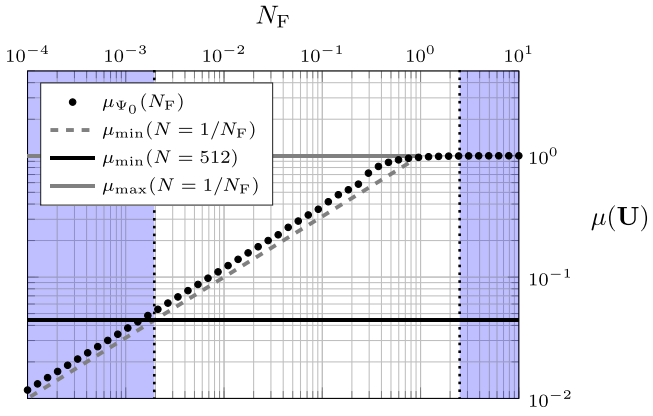

Fig. 2. Coherence between the wave propagation filter and the Shannon approximations at scale Δx as a function of N_F. The non-shaded area visualizes for which Fresnel numbers (6) is satisfied when $N = 512$, $\lambda = 633\,\mathrm{nm}$ and $\Delta x = 10\,\mu\mathrm{m}$.

and

$$b_0(\bar{x}, N_F) = \sqrt{2}\left(\bar{x}\sqrt{N_F} - \frac{1}{2\sqrt{N_F}}\right). \tag{15}$$

We denote by μ_{Ψ_0} the coherence between the wave propagation filter and the set Ψ_0. Since the sampling period along the $\bar{x}$-axis is 1, we find starting from (8), that

$$\mu_{\psi_0}(N_F) = \max_{n\in\mathbb{Z}} |y_{0,0}(n, N_F)| = \|y_{0,0}(n, N_F)\|_\infty, \tag{16}$$

where $|.|$ and $\|.\|_\infty$ denote respectively the modulus of a complex number and the infinity norm of a sequence. The infinity norm returns the global maximum of the modulus of a function and is invariant to scaling of the x-axis, which justifies our choice to express the wavelet responses as a function of $\bar{x}$ instead of x. Lastly, we obtain that

$$\mu_{\psi_0}(N_F) = \sqrt{\frac{N_F}{2}}\,\|F_r(a_0(n, N_F)) - F_r(b_0(n, N_F))\|_\infty \tag{17}$$

as a result of combining (13) and (16). A graphical representation of (17) is given in Fig. 2.

Validity of the wave propagation method: The validity of numerically propagating the angular spectrum is restricted to the Fresnel numbers that satisfy (6). Let us consider an interferometer with a HeNe-laser ($\lambda = 633$ nm), and an image sensor with $N = 512$ pixels and a pixel pitch $\Delta x = 10\,\mu$m. The non-shaded area in Fig. 2 represents the range of Fresnel numbers for which the numerical propagation of the angular spectrum is an accurate wave propagation model. We observe that $\mu_{\Psi_0}(N_F)$ tends to its lower bound $\mu_{\min}(N)$ as the Fresnel number goes to 0. However, the validity of numerically propagating the angular spectrum is bounded from below by $N_F > 1/N$. Thus, the range of valid Fresnel numbers and associated interferometer configurations increases as the number of pixels increases.

Limiting cases: If λ and Δx are fixed, then the propagation distance d is the only free parameter we can use to modify the Fresnel number. As d goes to 0, N_F goes to $+\infty$ and the wave propagation filter becomes an all-pass filter that leaves the phase unchanged. The sinc function $\psi_{0,0}(x)$, whose maximum modulus is equal to 1, is thus also the response. Hence, the coherence reaches its upper bound $\mu_{\max}(N) = 1$ and the (ℓ_0, ℓ_1)-equivalence is very weak, just as for classical photography where the image is a copy of the scene. The physical interpretation for d going to $+\infty$ is less obvious. We draw therefore on the right hand side of (17), whose numerator converges when N_F goes to 0. First, $a_0(n, N_F)$ becomes the additive inverse of $b_0(n, N_F)$ and both become independent of n. Secondly,

$$F_r(a_0(n, N_F)) - F_r(-a_0(n, N_F)) = 2F_r(a_0(n, N_F))$$

because the Fresnel integral is an odd function. And thirdly, the Fresnel integral converges to $(1 + j)/2$ as its argument goes to $+\infty$ [43]. As a result of these three properties and the observation that the bound in (17) is tight, we find that

$$\lim_{N_F \to 0} \mu_{\Psi_0}(N_F) = \sqrt{N_F}, \tag{18}$$

which matches the expression for the lower bound of the coherence when $N_F = N^{-1}$. Hence, the (ℓ_0, ℓ_1)-equivalence is strong when N_F and N approach 0 and $+\infty$ respectively. The expression in (18) is also the main result of [20], where approximations were used in the derivation. (We note that the definition of the coherence in [20] is slightly different from the one we use in (7), squaring the expression in (18) and multiplying by N is necessary for proper comparison). We have thus clarified that the results in [20] are only valid in the limit when N_F goes to 0. In practice, however, we have only a finite amount of pixels so the lower bound on the coherence is never reached. Resorting to the expression in (17) is therefore needful. In Fig. 2, for example, $\mu_{\Psi_0}(N_F = 1/512)$ is approximately 18% greater than $\mu_{\min}(N = 512) = 1/\sqrt{512}$. In spite of this observation, the (ℓ_0, ℓ_1)-equivalence can still be very strong [44].

C. Shannon Approximations at Coarser Scales

The framework we introduced in the previous subsection shows that impulses and Shannon approximations at the finest scale yield similar results for the coherence. However, the scaling functions are more likely composing a basis at a coarser scale in a multiresolution signal representation. The set

$$\Psi_k = \left\{\psi_{k,t}(x) = \frac{1}{\sqrt{2^k}}\,\mathrm{sinc}\left(\frac{(x - t2^k\Delta x)}{2^k\Delta x}\right)\right\}_{t\in\mathbb{Z}}$$

is an orthonormal basis for the Shannon approximations of square integrable functions at scale $2^k\Delta x$, where $k \in \mathbb{N}_0$. For determining the coherence between the wave propagation filter and the Shannon approximations at each scale, it is sufficient to calculate $y_{k,0}(x)$, which is the response of the wave propagation filter to $\psi_{k,0}(x)$.

The unitary Fourier transform of $\psi_{k,0}(x)$ is

$$\Psi_{k,0}(f_x) = \sqrt{2^k}\Delta x\,\mathrm{rect}\left(\Delta x 2^k f_x\right),$$

and the expression for $G_{\lambda,d}(f_x)\,\Psi_{k,0}(f_x)$ can be written as

$$\sqrt{2^k}\Delta x \exp\left[j\pi\frac{\lambda d}{2^{2k}}\left(2^k f_x\right)^2\right]\,\mathrm{rect}\left[\frac{2^k f_x}{2\left(\frac{1}{2\Delta x}\right)}\right].$$

We compare the latter expression with (9) and find that $W = (2\Delta x)^{-1}$, $\beta = \lambda d/4^k$, and f_x is replaced by $2^k f_x$. With the help of Theorem 1 and the time scaling property of the unitary Fourier transform, we obtain that $y_{k,0}(\bar{x}, N_F)$ is equal to

$$\frac{(F_r(a_k(\bar{x}, N_F)) - F_r(b_k(\bar{x}, N_F)))}{\sqrt{2^{1-k} N_F^{-1}} \exp(+j\pi N_F \bar{x}^2)}, \tag{19}$$

where

$$a_k(\bar{x}, N_F) = \sqrt{2}\left(\frac{\bar{x}}{2^k}\sqrt{4^k N_F} + \frac{1}{2\sqrt{4^k N_F}}\right), \tag{20}$$

and

$$b_k(\bar{x}, N_F) = \sqrt{2}\left(\frac{\bar{x}}{2^k}\sqrt{4^k N_F} - \frac{1}{2\sqrt{4^k N_F}}\right). \tag{21}$$

In (20), we have organized the factors in such a way that it is clear that

$$a_k(\bar{x}, N_F) = a_0\left(\frac{\bar{x}}{2^k}, 4^k N_F\right), \tag{22}$$

where a_0 is defined in (14). A similar equality exists between (15) and (21). We can rewrite (19), consequently, as

$$\frac{F_r\left(a_0\left(\frac{n}{2^k}, 4^k N_F\right)\right) - F_r\left(b_0\left(\frac{n}{2^k}, 4^k N_F\right)\right)}{\sqrt{2^{k+1}(4^k N_F)^{-1}} \exp(+j\pi N_F \bar{x}^2)}, \tag{23}$$

where we denote by μ_{Ψ_k} the coherence between the wave propagation filter and the set Ψ_k. Starting from (23) and by analogy with (16), we find the expression for $\mu_{\Psi_k}(N_F)$ is

$$\frac{\left\|F_r\left(a_0\left(\frac{n}{2^k}, 4^k N_F\right)\right) - F_r\left(b_0\left(\frac{n}{2^k}, 4^k N_F\right)\right)\right\|_\infty}{\sqrt{2^{k+1}(4^k N_F)^{-1}}}. \tag{24}$$

The arguments of the Fresnel integrals in (13) and (23) are scaled with respect to each other, but the result of the infinity norm is quasi not affected by this operation because the sampling is dense enough for $k = 0$ and densifies by a factor 2 each time the scale of the approximation functions doubles. As a result, we obtain the approximation

$$\mu_{\psi_k}(N_F) \approx \frac{1}{\sqrt{2^k}} \mu_{\psi_0}(4^k N_F). \tag{25}$$

The coherence between the wave propagation filter and the Shannon approximations is thus scaled and shifted when the scale gets coarser. In the limiting case where $N_F = N^{-1}$ and N goes to $+\infty$, the coherence as a function of N_F becomes a straight line in double logarithmic axes, which is obvious in Fig. 2. The numerator in (24) converges to $(1 + j)/2$ when N_F goes to 0 for the same reason as in the previous subsection. In this limiting case, (25) becomes

$$\lim_{N_F \to 0} \mu_{\psi_k}(N_F) \approx \lim_{N_F \to 0} \frac{1}{\sqrt{2^k}} \mu_{\psi_0}(4^k N_F) \tag{26}$$

$$\approx \frac{1}{\sqrt{2^k}} \sqrt{4^k N_F}, \tag{27}$$

where (27) is the result of substituting (18) in (26). Finally, we substitute $N_F = N^{-1}$ in (27) and find that

$$\lim_{N_F \to 0} \mu_{\Psi_k}(N_F) = \frac{1}{\sqrt{2^k}} \sqrt{\frac{4^k}{N}} = \sqrt{2^k} \mu_{\min}(N). \tag{28}$$

Coarser approximation functions yield thus higher values for the coherence. Finally, if $N_F = N^{-1}$, then we can rewrite (28) as

$$\lim_{N_F \to 0} \mu_{\Phi_k}(N_F) = \lim_{N_F \to 0} \mu_{\Phi_0}(2^k N_F). \tag{29}$$

As N_F approaches 0, doubling the scale of the Shannon approximations has thus the same effect on the coherence as halving the wave length, halving the free-space propagation distance, or doubling the area of a pixel.

D. Shannon Wavelets

Wavelets capture the details that are lost when approximating a square integrable function at a certain scale. In particular, the spectrum of the mother Shannon wavelet is [45]

$$\begin{cases} \exp(-j\pi\Delta x f_x) & \text{if } f_x \in [-1, -1/2] \cup [1/2, 1] \\ 0 & \text{otherwise.} \end{cases} \tag{30}$$

When we ignore the phase information in (30), it becomes clear that the amplitude spectrum of a Shannon wavelet is a linear combination of the spectra of the Shannon approximation functions at neighbouring scales. Let $\psi_{k,t}^{k+1}(x)|_{t \in \mathbb{Z}}$ be the set of wavelets that carry the details for complementing the approximation at scale $2^{k+1}\Delta x$ in order to get an approximation at scale $2^k \Delta x$, which is finer. The wavelet $\psi_{k,0}^k(x)$ is a representative for all its translations at the same scale and its unitary Fourier transform is given by

$$\Psi_{k,0}^{k+1}(f_x) = \sqrt{2}\Psi_{k,0}(f_x) - \Psi_{k+1,0}(f_x)$$

since we do not take into account the phase information for now. As a result of the superposition principle we find that the response of the propagation filter to $\psi_{k,0}^{k+1}(x)$ is

$$y_{k,0}^{k+1}(\bar{x}, N_F) = \sqrt{2} y_{k,0}(\bar{x}, N_F) - y_{k+1,0}(\bar{x}, N_F).$$

The complex exponential in (30) causes a shift of the samples by $\Delta x/2$ on the x-axis or $1/2$ on the $\bar{x}$-axis. Consequently, the coherence between the wave propagation filter and the set $\psi_k^{k+1}(x)|_{z \in \mathbb{Z}}$ is

$$\mu_{\psi_k^{k+1}}(N_F) = \Big\| \sqrt{2} y_{k,0}(n - 1/2, N_F) - y_{k+1,0}(n - 1/2, N_F) \Big\|_\infty. \tag{31}$$

Shannon wavelets inherit the scaling and shifting rules from Shannon approximation functions, so

$$\mu_{\Psi_k^{k+1}}(N_F) \approx \frac{1}{\sqrt{2^k}} \mu_{\Psi_0^1}(4^k N_F).$$

Furthermore, the triangle inequality states that

$$\left\| \sqrt{2} y_{k,0} - y_{k+1,0} \right\|_\infty \le \sqrt{2} \left\| y_{k,0} \right\|_\infty + \left\| y_{k+1,0} \right\|_\infty, \tag{32}$$

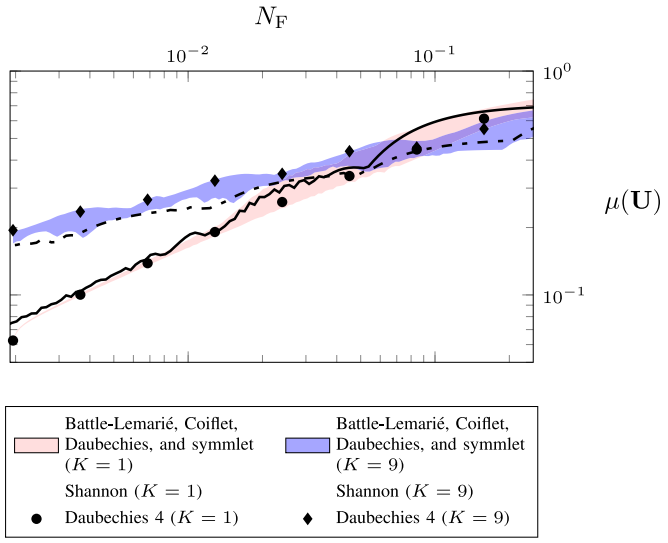

Fig. 3. Coherence between the wave propagation filter and the Shannon multiresolution representation, as well as the finite-interval Battle-Lemarié, Coiflet, Daubechies, and symmlet multiresolution representations for $K \in \{1, 9\}$.

where $\|y_{k,0}(n - 1/2, N_F)\|_\infty = \mu_{\Psi_k}(N_F)$. By taking the limit of (31) as N_F goes to 0, then applying inequality (32) and taking (28) into account, we find that

$$\lim_{N_F \to 0} \mu_{\Psi_k^{k+1}}(N_F) \leq \sqrt{2^{k+3}}\mu_{\min}(N) \tag{33}$$

when $N_F = N^{-1}$. Wavelets that complement the approximation at scale $2^{k+1}\Delta x$ yield thus a coherence that is maximum 2 times greater than the coherence for the approximation functions.

E. Shannon Multiresolution Representation

Wavefields are sparse in a multiresolution representation rather than at a single scale. Therefore, we still have to combine the results in (24) and (31). Let μ_K be the coherence between the wave propagation filter and the Shannon multiresolution representation at the $(K + 1)$ finest scales. By analogy with the definition of the coherence in (7), we find that

$$\mu_K(N_F) = \max\left(\mu_{\Psi_K}(N_F), \mu_{\Psi_{K-1}^K}(N_F), \cdots, \mu_{\Psi_1^2}(N_F)\right),$$

which is visualized in Fig. 3 for $K = 1$ and $K = 9$. We observe that the coherence follows a bumpy, but overall decreasing trend as N_F decreases. We will discuss this behaviour on the basis of physical arguments in Section IV-B. Here, we consider the limiting case where $N_F = N^{-1}$ and N goes to $+\infty$ from a mathematical perspective. $\mu_K(N_F)$ is the maximum of (28) and (33) for respectively $k = K$ and $k = K - 1, K - 2, \cdots, 0$. As a result, we find that

$$\lim_{N_F \to 0} \mu_K(N_F) \leq \sqrt{2^{K+2}}\mu_{\min}(N), \tag{34}$$

which is a valid inequality as long as N is sufficiently large.

Furthermore, we compute the coherence for a discrete 512-dimensional vector space and all Battle-Lemarié, coiflet, Daubechies and symmlet multiresolution representations in the *Wavelab* package [46]. We see in Fig. 3 that the coherence curves for all these representations lie in a region that gets tighter as N_F decreases. The blue and red regions are narrow because the coherence is not very sensitive to the specific type of wavelet. The common formulation of the time-frequency analysis can be an explanation for this observation. Furthermore, the overall trend is predicted well by $\mu_K(N_F)$, although our analysis is targeted at integrable functions in the continuous domain. The coherence is thus more sensitive to N_F and K than the specific type of wavelet.

IV. Phase Transition Bounds

The coherence explains global trends, which are similar for all aforementioned wavelet transforms, but for accurate and precise bounds on the (ℓ_0, ℓ_1)-equivalence we have to resort to phase transition bounds. Generating them is very computationally intensive. We select therefore the Daubechies 4 wavelet transform as a representative. Adhering to the previous section, all experiments are executed with $\mathbf{\Phi}_{\mathbf{N_F}}$ as sensing operator, the Daubechies 4 wavelet transform on a finite interval as sparsifying operator, and 1-D wavefields in an N-dimensional vector space, where $N = 512$.

A. Generation of Phase Transition Diagrams

We generate a phase transition diagram for each of the 8 Fresnel numbers that are identified by the abscissae of the disks (•) and diamonds (♦) in Fig. 3. On a logarithmic N_F-axis, they are evenly distributed over the interval where (6) is satisfied, $N_F = N^{-1}$ included. Furthermore, we consider the Daubechies 4 wavelet transform at a minimum ($K = 1$), as well as a maximum [$K = \log_2(512) = 9$] number of scales.

For the generation of a phase transition diagram, the phase-space is sampled in all doubles of the set $\{(\delta(d), \rho(r))\}_{d,r=1}^{50}$, where $\delta(d) = 0.02d$ and $\rho(r) = 0.02r$. In each of these samples we consider the associated set of sparse signals with sparsity $S(d, r) = \lceil N\delta(d)\rho(r) \rceil$. For the generation of sparse signals we select $S(d, r)$ out of N indices uniformly at random without replacement. These indices are labelled as the positions of significant wavelet coefficients, which are drawn from a zero-mean circularly-symmetric complex normal distribution with a variance of 2. Thereafter, we normalize all sparse signals so that they have unit Euclidean norms.

By means of (3), we transform an $S(d, r)$-sparse signal $\mathbf{x}$ into the corresponding hologram $\mathbf{h}$. Then, we select $N\delta(d)$ hologram samples pseudo-uniformly at random and store them in vector $\mathbf{y}$, which we refer to as the linear measurements or observations in optimization problem ($\mathrm{P}_{p,\epsilon}$). For the reconstruction of $\mathbf{x}$ from $\mathbf{y}$, we solve the ℓ_1-minimization problem ($\mathrm{P}_{1,0}$) by making use of the SDPT3 solver.[1]

If the mean squared error between the original and reconstructed signals is smaller than 1×10^{-12}, we deem the reconstruction is correct. For each phase-space sample $(\delta(d), \rho(r))$, we execute 50 reconstructions and $E(d, r)$ of them are deemed

[1]The SDPT3 solver [47] is included in the CVX distribution [48]. We used the default settings for complex-valued problems as described in CVX's documentation [49].

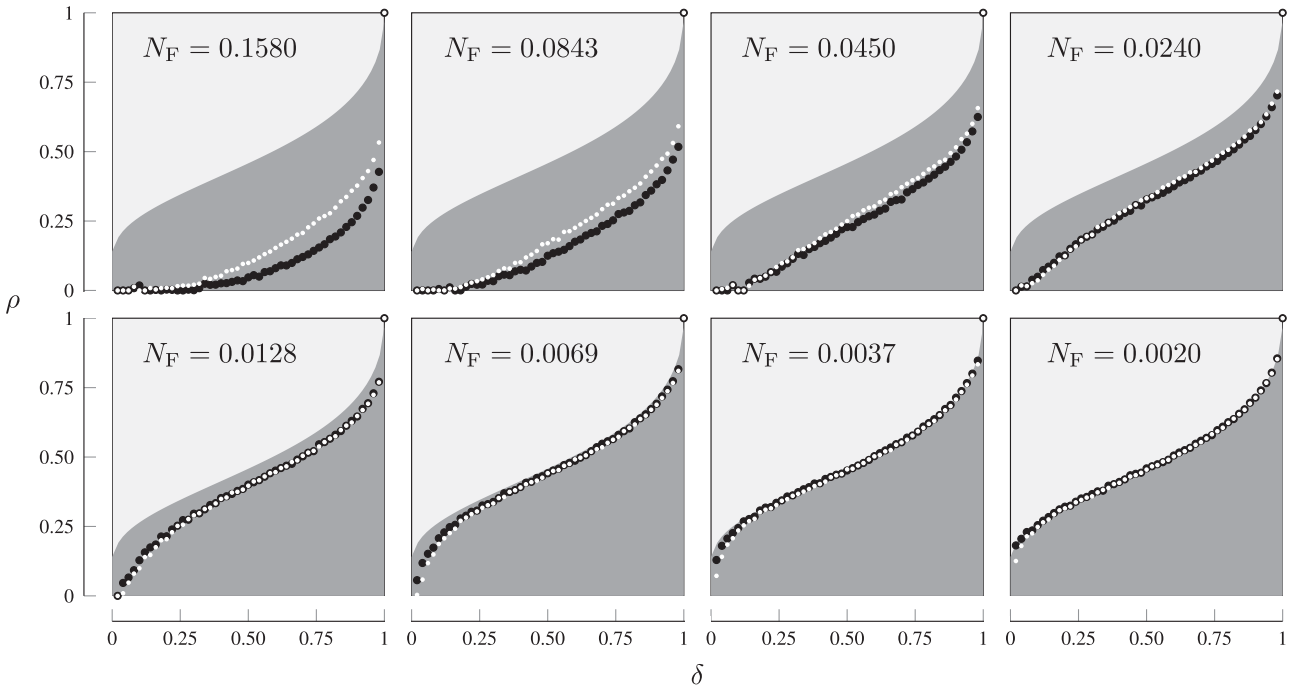

Fig. 4. Phase transition bounds as a function of the Fresnel number for compressed holography with the Daubechies 4 wavelet transform as sparsifying operator. The (ℓ_0, ℓ_1)-equivalence region under the optimal phase transition bound is shaded dark-grey, and the black and white dots represent samples of the phase transition bounds for $K = 1$ and $K = 9$ respectively.

exact. The sampled phase transition diagram is then estimated by $\hat{\pi}(\delta(d), \rho(r)) = E(d, r)/50$. By using a logistic regression model and following the procedure in [33], [50], we obtain an estimate for the phase transition bound $\hat{\rho}_{0.5}(\delta)$.

B. Analysis of the (ℓ_0, ℓ_1)-Equivalence

The phase transition bounds that correspond with the disks and diamonds in Fig. 3 are depicted with respectively black and white dots in Fig. 4. We observe that the decreasing trend in the coherence, as the Fresnel number decreases, yields a stronger (ℓ_0, ℓ_1)-equivalence. Furthermore, the analysis of the coherence predicts that the geometrical position of the phase transition bound is dependent on K. For large Fresnel numbers, the coherence for $K = 9$ is slightly smaller than for $K = 1$. The gap between the corresponding phase transition bounds is significant nevertheless. A possible explanation for this behaviour might be hidden in the wave propagation phenomenon. We can namely state that the Fresnel number, which is a measure for the amount of diffraction, is roughly inversely proportional to the radius of a circle of confusion in the hologram plane due to a source with a small support in the object plane. Imaging modalities that are characterized by a large Fresnel number are less prone to blurring and the image is accordingly an (exact) copy of the object, which is the case in classical photography. As a consequence, the wavelets are projected onto themselves and the peaks in the finest approximation functions and wavelets pull the coherence upwards. Our coherence study and phase transition diagrams confirm the weak (ℓ_0, ℓ_1)-equivalence for a measurement matrix $\mathbf{U}$ that is simply an inverse discrete wavelet transform by itself [51]. Since the rather flat, wide wavelets at coarser scales are less coherent with the identity matrix than the narrow, peaked wavelets at the finest scale, there is locally a drop in the coherence, which can be an explanation for the stronger (ℓ_0, ℓ_1)-equivalence as K increases.

When the Fresnel number decreases, the energy of a source with a small support is spread out over an extending circle of confusion. The same happens with the wavelets at the finest scale. They are smeared over an extending support size due to diffraction, which reduces their peakedness and decreases the coherence as depicted in Fig. 2. The wavelets at the second finest scale are not yet affected by diffraction so the coherence between them and the wave propagation filter remains quasi unchanged. As a result, the overall coherence drops until the wavelets at the second scale become most coherent with the wave propagation filter. Dividing the Fresnel number by 4 [cfr. the factor 4^k in (23)] at this point causes the wavelet responses at the second finest scale to spread out on their turn while the coherence between the wavelets at the finest scale and the wave propagation filter continues to decrease at a rate of 10 dB per decade on the N_F-axis [see (24) and (25)]. Since this pattern is repeated at the coarser scales each time the Fresnel number is divided by 4, we can explain the bumpy decay of the coherence when $K = 9$, as well as the decay when $K = 1$ as N_F goes to 0, see Fig. 2.

So far, the coherence and physical arguments have been helpful for explaining the global trends in the phase transition bounds, but they cannot accurately quantify them. In particular, we observe that both phase transition bounds tend to the weak threshold for block-sparse compressive sensing [24], [52] with a block length of 2. This bound is derived for real-valued measurement matrices with normally distributed elements, but several

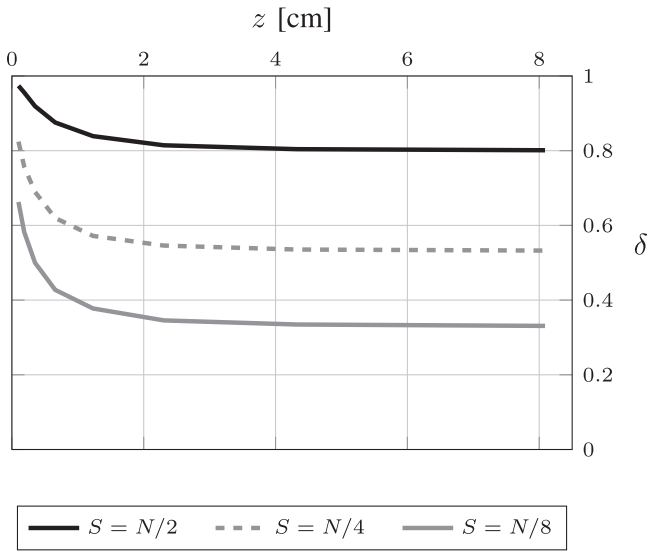

Fig. 5. Minimum undersampling factor to recover S-sparse wave fields perfectly, as a function of the free-space propagation. Three values of S are distinguished and $N = 512$.

TABLE I
THE P-VALUES FOR 8 (N, N_F, K)-TUPLES*

	$N = 512$				$N = 1024$			
	$N_F = 1/256$		$N_F = 1/512$		$N_F = 1/512$		$N_F = 1/1024$	
δ	$K = 1$	$K = 9$	$K = 1$	$K = 9$	$K = 1$	$K = 9$	$K = 1$	$K = 9$
0.1	**0.60**	**0.00**	61.8	**0.60**	**0.33**	**0.00**	13.5	**0.02**
0.2	**1.76**	**0.18**	95.6	**4.43**	46.0	**1.76**	75.8	9.67
0.3	**1.76**	**0.18**	**4.43**	**2.84**	75.8	**0.04**	54.0	18.4
0.4	**0.33**	**0.02**	30.9	30.9	30.9	**0.01**	**4.43**	13.5
0.5	69.1	**4.43**	30.9	9.67	18.4	**4.43**	24.2	18.4
0.6	**0.04**	**1.05**	38.2	13.6	24.2	18.4	**4.43**	54.0
0.7	6.66	**1.76**	46.0	**1.05**	**4.43**	**0.09**	46.0	**1.05**
0.8	46.0	**0.04**	93.3	13.6	13.6	**4.43**	81.6	46.0
0.9	13.6	**0.18**	61.8	**0.04**	**2.84**	**0.60**	46.0	18.4

*All p-values are expressed as percentages. The p-values that are smaller than 5% are printed in bold type. And those that are smaller than 1% are in addition printed on a grey background.

complex-valued, deterministic matrices are associated with the same phase transition bound for large N [53]. We denote this phase transition bound by $\rho^*_{0.5}(\delta)$ and it coincides in Fig. 4 with the edge between the light- and darkgrey regions. The fact that the phase transition bounds for compressive digital holography can lie very close to $\rho^*_{0.5}(\delta)$ cannot be predicted by means of the coherence and justifies the computational effort required to generate phase transition diagrams.

Let us, to complete this Subsection, compare the trends in our results (using the Daubechies 4 wavelet transform) with those in [54], where the Haar, Coiflet 1, and symmlet 2 wavelet transforms are considered. Therefore, we consider the points on the phase transition bounds for $K = 9$ that correspond with S-sparse wavefields, for $S \in \{N/2, N/4, N/8\}$, where $N = 512$. The undersampling factors of these points are plotted versus the free-space propagation distance z, which can be derived from the Fresnel number using the formula $z = (\Delta x)^2/(\lambda N_F)$, where $\lambda = 633$ nm and $\Delta x = 10\,\mu$m. The result is depicted in Fig. 5, and they show the same trends as in [54, Fig. 2]. The undersampling factor δ has M in the nominator and represents thus the amount of required measurements to reconstruct the wave fields perfectly; an amount that tends to decrease as the free-space propagation distance is increased. The minimum in the near field is reached for the maximum propagation distance that we have included in Fig. 5, but the sensitivity of δ around that propagation distance is low, indicating that precise positioning of the camera with respect to the object is not necessary. Finally, the amount of required measurements decreases as S decreases.

C. Optimal (ℓ_0, ℓ_1)-Equivalence

Naturally, the question arises whether $\rho^*_{0.5}(\delta)$ is actually the isoline that is associated with $\hat{\pi} = 0.5$ in compressive digital holography with an orthogonal wavelet transform as sparsifying operator when $N_F = N^{-1}$ and N goes to $+\infty$. Even though N has to go to $+\infty$ from a statistical perspective, the universality of $\rho^*_{0.5}(\delta)$ has been demonstrated for multiple deterministic, complex-valued compressive sensing problems where N is smaller than 1024 [44], [55]. We adopt this strategy for compressive digital holography and advocate the following null hypothesis: $\rho^*_{0.5}(\delta)$ is the isoline that is associated with $\hat{\pi} = 0.5$. By means of a single-tailed proportion test on a Bernouilli distribution, evidence is collected for the alternative hypothesis: the isoline that is associated with $\hat{\pi} = 0.5$ is strictly bounded from above by $\rho^*_{0.5}(\delta)$.

We execute 100 independent reconstructions in the phase-space doubles $(d/10, \rho^*_{0.5}(d/10))$ for $d = 1, 2, \cdots, 9$ and evaluate the hypothesis test in each point with regard to the 5% and 1% significance levels. The results are shown in Table I, where the p-values are summarized for 8 configurations of the interferometer.

We refute the null hypothesis when $N_F = (N/2)^{-1}$ and $K = 9$ because the evidence against the null-hypothesis is significant. We base this thesis on a majority of p-values that are smaller than the significance levels. For (N, N_F, K)-triples that match the templates $(N, (N/2)^{-1}, 1)$ or $(N, N^{-1}, 9)$, the p-values in Table I indicate that the phase transition bound is below $\rho^*_{0.5}(\delta)$ for a substantial amount of undersampling rates, but no majority. However, we behave as if $\rho^*_{0.5}(\delta)$ is the phase transition bound for the triples that match $(N, N^{-1},1)$ because there is insufficient evidence against the null-hypothesis [i.e., the p-values are in general much greater than 5% and the alternative hypothesis is more likely in merely a few samples of $\rho^*_{0.5}(\delta)$]. Since $\rho^*_{0.5}(\delta)$ is also associated with acquiring measurements in the frequency domain of objects that are sparse in the spatial domain [55], we conclude that in this case the hologram samples in $\mathbf{y}$ are as informative as compressive measurements in the frequency domain, thereby making the link with Fourier-based imaging systems like magnetic resonance imaging and synthetic aperture radar.

Although the optimal (ℓ_0, ℓ_1)-equivalence is only feasible in specific circumstances, we notice that the phase transition bound is in the near proximity of $\rho^*_{0.5}(\delta)$ for all configurations where N_F goes to N^{-1}. Since other wavelet transforms yield similar results for the coherence as the Daubechies 4 wavelet transform, we can assume that the trends for the phase transition bounds are similar too. The choice for a specific wavelet transform has therefore a larger impact on the sparsity of the object wavefield (i.e., smaller values for S) than the phase transition bound.

D. Extension to 2-D Wavefields

Eventually, we are interested in the reconstruction of 2-D sparse wavefields, but the SDPT3 solver is not appropriate for large-scale optimization problems. We employ therefore the SPGL1 solver [56], [57], which converges much faster and has been used before in complex-valued compressive sensing problems [58], though admittedly it is slightly less performant than the SDPT3 solver.

Since the wave propagation filter and all orthogonal wavelet transforms are separable, the coherence for the 2-D case is the square of the coherence for the 1-D case, which means the decreasing trend in the coherence is preserved as N_F decreases. Consequently, we expect the strongest (ℓ_0, ℓ_1)-equivalence for $N_F = N^{-1}$, where N is the number of samples along each side of the wavefield. We demonstrate the dependence of the reconstruction error on N_F by means of visual features. The 2-D wavefield of a USAF resolution test chart is reconstructed from randomly-undersampled holograms ($\delta = 0.2$) that were captured with a Ximea MD120MU-SY camera. The reconstructions for 3 different Fresnel numbers are shown in Fig. 6 and the reconstruction error clearly decreases as the Fresnel number decreases.

E. Implications for Compressive Digital Holography

We learn from our analysis that the wave propagation phenomenon (diffraction) can be incorporated as a sensing operator in compressive sensing. In combination with an arbitrary orthogonal wavelet transform as sparsifying operator, the measurement matrix is associated with the same phase transition bound as for Gaussian random matrices in combination with block-sparse real-valued signals with a block length of 2. The numerical back propagation method requires N^r hologram samples to reconstruct an r-D object wavefield. However, for compressive digital holography we find the following rule of thumb: if we can sparsify the object wavefield such that $S = N^r/k^2$ for $k \in [3, 10]$, then N^r/k measurements are sufficient. Sparse priors allow thus for measurement reductions. To accomplish this, the interferometer has to be configured such that the condition $N_F = N^{-1}$ is (approximately) satisfied. Practical applications as those in the introduction do not undersample the hologram uniformly at random, but the interferometer should still be configured such that N_F is as close to N^{-1} as possible. This way, the phase transition bound has the largest margin to become weaker without the need to constrain the set of object wavefields to just the extreme sparse ones.

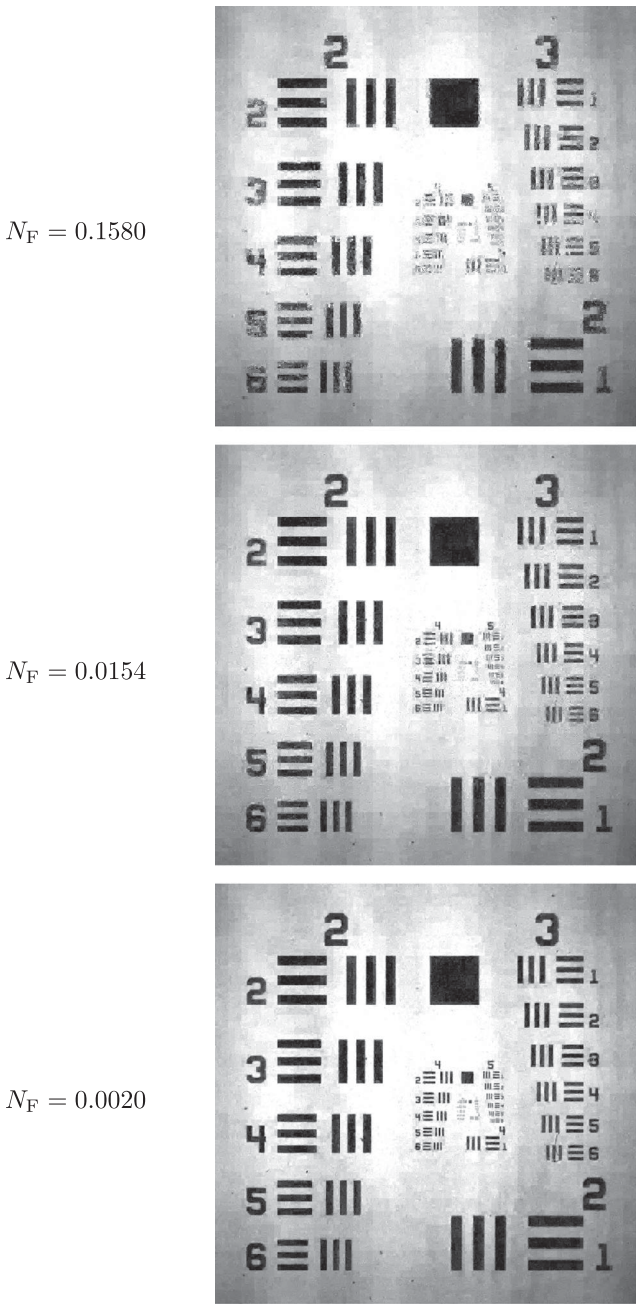

Fig. 6. Reconstructions of a USAF resolution test chart's wavefield in a holographic recording setup for $\delta = 0.2$ and different Fresnel numbers. Smaller Fresnel numbers correspond with smaller reconstruction errors.

V. Laboratory Experiments

We conducted a real-life experiment to demonstrate that the reconstructed object wavefields are robust to sparsity defects, vibrations in the interferometer, energy that misses the image sensor, and additive noise. The diameter of the HeNe-laser's beam (JDSU Uniphase 1135P) was expanded to 1.5 cm for illuminating the transmissive angle grid (on the multi-grid standard

stage micrometer of Edmund Optics). We recorded in a Mach-Zehnder interferometer 3 phase-shifted interferograms I_1, I_2, and I_3, where

$$I_k(x,y) = \left|h(x,y) + R(x,y)\exp\left(jk\frac{\pi}{2}\right)\right|^2 + e_k(x,y),$$

$R(x,y)$ is the amplitude profile of the reference wave, and $e_k(x,y)$ is an error term. With the pointwise three-step linear combination [5]

$$\frac{1-j}{4R(x,y)}\left\{I_0(x,y) - I_1(x,y) + j\left[I_1(x,y) - I_2(x,y)\right]\right\},$$

we retrieved a distorted hologram. The phase of the reference wave was modified with a piezo-electrically driven mirror, and the interferograms were captured with a Ximea MD120MU-SY camera (4244×2832 image sensor resolution). The pixel pitch of this camera is $3.1\,\mu$m, but we generated superpixels consisting of 3 by 3 pixels, which yields a $9.3\,\mu$m pixel pitch. We also reduced the camera size artificially to 640×448 superpixels, which is slightly smaller than the support of the 768×544 angle grid's hologram so that the number of hologram samples is not excessive. The distance between the angle grid and the camera was 7.6 cm. The interferometer is thus characterized by $N_F = 0.0018$, which is slightly smaller than $1/448$, thereby producing a little aliasing, which is sufficiently small to be invisible in the reconstruction.

We observe in Fig. 7(a) that zero-padding the hologram, followed by numerical back propagation results in a distorted reconstruction near the edge of the image sensor. Zero-padding imposes namely that the hologram should have a finite support, which is not a realistic assumption. We tested several border extension methods and came to the conclusion that the border should be repeated for specimen that are transparent near the edge of the image sensor. Even the engraving "15 °", which overlaps partially with the edge of the image sensor, is accurately reconstructed, as illustrated in Fig. 7(b). We consider this reconstruction therefore as a reference.

The angle grid's object wavefield is clearly not sparse in the spatial domain. Selecting the identity transformation for $\mathbf{\Psi}$ results accordingly in very poor reconstructions [see Fig. 7(c) and (d)]. These experiments should make the need for (orthogonal) wavelet transforms and corresponding bounds on the (ℓ_0, ℓ_1)-equivalence clear.

On the other hand, the angle grid is sparse in a symmlet 6 multiresolution representation for $K = 5$ [$\rho = S/(640 * 440) = 0.032$]. When we discard 75 or even 90% of the hologram samples, the characters of the string "15 °" are still engraved near the top edge of the detector in Fig. 7(e) and (f), just as for the reference using border repetition and numerical back propagation. In contrast, the degrees symbol protrudes from the background for the numerical back propagation method following zero-padding [see Fig. 7(a)]. Finally, we observe for compressive digital holography with the symmlet 6 wavelet transform that the main structures of the angle grid are preserved, even near the edges of the image sensor. The reconstruction is thus robust to additive noise, vibrations, and a part of the hologram that misses the image sensor.

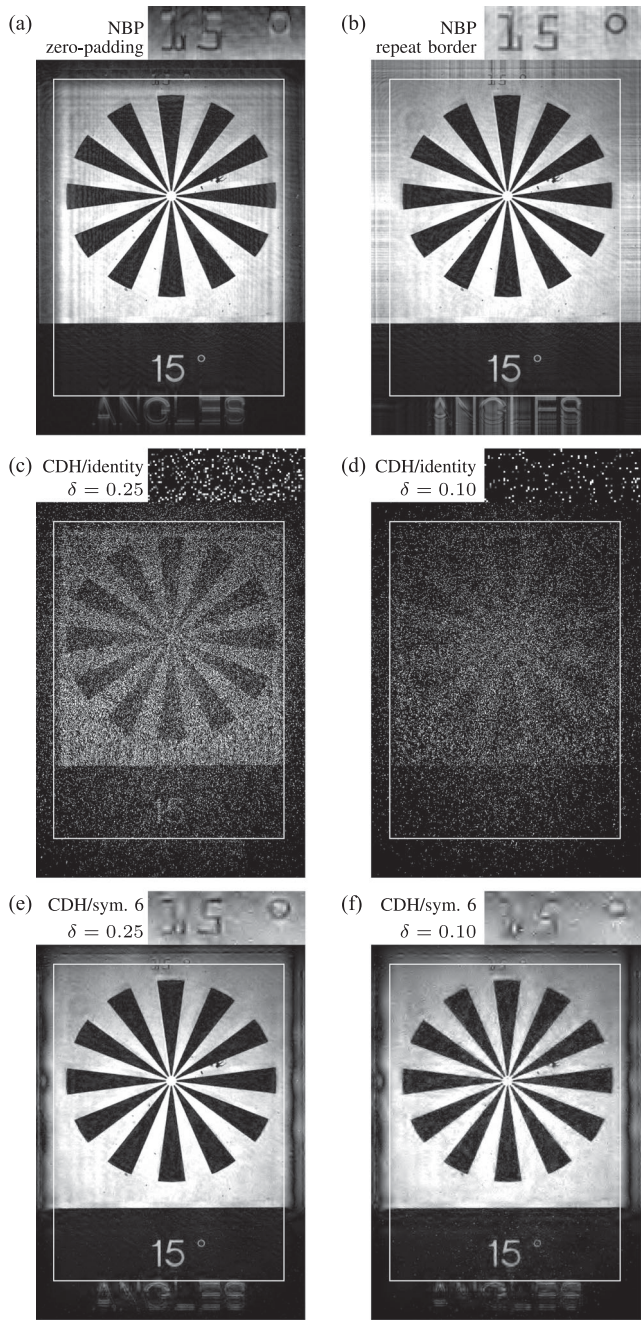

Fig. 7. Reconstructions of the object wavefield of an angle grid using the Numerical Back Propagation (NBP) method with different border extensions [(a), (b)], and Compressive Digital Holography (CDH) with the canonical basis [(c), (d)] and symmlet 6 wavelets [(e), (f)] as sparsifying operator, for $\delta = 0.25$ and 0.10. Magnified views of the engraving "15 °" near the top of the angle grid are shown in the upper right corners and the edge of the detector is marked with a white rectangle.

VI. Conclusion

Our coherence analysis has linked the physical aspects of the wave propagation phenomenon to the reconstruction error in compressive digital holography for wavefields that are sparse in a generic multiresolution orthogonal wavelet representation and randomly undersampled holograms. Unlike ray-based imaging, a sufficient amount of diffraction yields appropriate sensing

operators for compressive sensing. In particular, we have shown that the interferometer should be configured such that the Fresnel number is equal to the inverse of the number of pixels along 1 dimension of the sensor. In this context, we confirmed the following thesis: the phase transition bound coincides with the weak threshold for block-sparse compressive sensing with a block length of 2.

ACKNOWLEDGMENT

The authors are grateful to the Brussels Photonics team for the optical equipment and in particular to Prof. Heidi Ottevaere for the instructions on how to align the interferometer.

REFERENCES

[1] F. Dubois, C. Yourassowsky, N. Callens, C. Minetti, and P. Queeckers, "Applications of digital holographic microscopes with partially spatial coherence sources," *Proc. J. Phys., Conf. Ser.*, vol. 139, no. 1, 2008, Art. no. 012027.

[2] F. Charrière *et al.*, "Characterization of microlenses by digital holographic microscopy," *Appl. Opt.*, vol. 45, no. 5, pp. 829–835, 2006.

[3] K. D. Hinsch, "Holographic particle image velocimetry," *Meas. Sci. Technol.*, vol. 13, no. 7, pp. R61–R72, 2002.

[4] T. Kreis, *Handbook of Holographic Interferometry: Optical and Digital Methods*. Hoboken, NJ, USA: Wiley-VCH, 2005.

[5] T.-C. Poon, Ed., *Digital Holography and Three-Dimensional Display*, 1st ed. New York, NY, USA: Springer, 2006.

[6] J. W. Goodman, *Introduction to Fourier Optics*, 2nd ed. New York, NY, USA: McGraw-Hill, 1996.

[7] P. Clemente, V. Durán, E. Tajahuerce, P. Andrés, V. Climent, and J. Lancis, "Compressive holography with a single-pixel detector," *Opt. Lett.*, vol. 38, no. 14, pp. 2524–2527, 2013.

[8] D. L. Donoho, "For most large underdetermined systems of linear equations the minimal l1-norm solution is also the sparsest solution," *Commun. Pure Appl. Math.*, vol. 59, no. 6, pp. 797–829, 2006.

[9] E. J. Candès and M. B. Wakin, "An introduction to compressive sampling," *IEEE Signal Process. Mag.*, vol. 25, no. 2, pp. 21–30, Mar. 2008.

[10] S. Foucart and H. Rauhut, *A Mathematical Introduction to Compressive Sensing* (Applied and Numerical Harmonic Analysis), 1st ed. Basel, Switzerland: Birkhäuser, 2013.

[11] L. Williams, G. Nehmettallah, and P. P. Banerjee, "Digital tomographic compressive holographic reconstruction of three-dimensional objects in transmissive and reflective geometries," *Appl. Opt.*, vol. 52, no. 8, pp. 1702–1710, 2013.

[12] D. J. Brady, K. Choi, D. L. Marks, R. Horisaki, and S. Lim, "Compressive holography," *Opt. Express*, vol. 17, no. 15, pp. 13040–13049, 2009.

[13] K. Choi *et al.*, "Compressive holography of diffuse objects," *Appl. Opt.*, vol. 49, no. 34, pp. H1–H10, 2010.

[14] J. Hahn, S. Lim, K. Choi, R. Horisaki, and D. J. Brady, "Video-rate compressive holographic microscopic tomography," *Opt. Express*, vol. 19, no. 8, pp. 7289–7298, 2011.

[15] A. Symeonidou, D. Blinder, A. Munteanu, and P. Schelkens, "Computer-generated holograms by multiple wavefront recording plane method with occlusion culling," *Opt. Express*, vol. 23, no. 17, pp. 22149–22161, 2015.

[16] R. Horisaki, Y. Ogura, M. Aino, and J. Tanida, "Single-shot phase imaging with a coded aperture," *Opt. Lett.*, vol. 39, no. 22, pp. 6466–6469, 2014.

[17] R. Horisaki, R. Egami, and J. Tanida, "Experimental demonstration of single-shot phase imaging with a coded aperture," *Opt. Express*, vol. 23, no. 22, pp. 28691–28697, 2014.

[18] T. Egami, R. Horisaki, L. Tian, and J. Tanida, "Relaxation of mask design for single-shot phase imaging with a coded aperture," *Appl. Opt.*, vol. 55, no. 8, pp. 1830–1837, 2016.

[19] C. Schretter *et al.*, "Compressed digital holography: From micro towards macro," *Proc. SPIE*, vol. 9971, 2016, Art. no. 99710V.

[20] Y. Rivenson and A. Stern, "Conditions for practicing compressive fresnel holography," *Opt. Lett.*, vol. 36, no. 17, pp. 3365–3367, 2011.

[21] M. Liebling, T. Blu, and M. Unser, "Fresnelets: New multiresolution wavelet bases for digital holography," *IEEE Trans. Image Process.*, vol. 12, no. 1, pp. 29–42, Jan. 2003.

[22] S. Bettens, H. Yan, S. Bundervoet, C. Schretter, A. Dooms, and P. Schelkens, "Reconstruction resilience to subsampling in compressive Fresnel holography," in *Proc. Digit. Holography 3-D Imag. Meeting*, 2015, Paper DT1A.3.

[23] S. Bettens, H. Yan, D. Blinder, H. Ottevaere, C. Schretter, and P. Schelkens, "Studies on the sparsifying operator in compressive digital holography," *Opt. Express*, vol. 25, no. 16, pp. 18656–18676, 2017.

[24] M. Stojnic, F. Parvaresh, and B. Hassibi, "On the reconstruction of block-sparse signals with an optimal number of measurements," *IEEE Trans. Signal Process.*, vol. 57, no. 8, pp. 3075–3085, Aug. 2009.

[25] S. Silver, "Microwave aperture antennas and diffraction theory," *J. Opt. Soc. Amer.*, vol. 52, no. 2, pp. 131–139, 1962.

[26] D. Voelz, *Computational Fourier Optics: A MATLAB Tutorial*. Bellingham, WA, USA: SPIE Press, 2011.

[27] E. J. Candès, J. Romberg, and T. Tao, "Robust uncertainty principles: Exact signal reconstruction from highly incomplete frequency information," *IEEE Trans. Inf. Theory*, vol. 52, no. 2, pp. 489–509, Feb. 2006.

[28] J. A. Tropp, "Just relax: Convex programming methods for identifying sparse signals in noise," *IEEE Trans. Inf. Theory*, vol. 52, no. 3, pp. 1030–1051, Mar. 2006.

[29] G. M. Fung and O. L. Mangasarian, "Equivalence of minimal ℓ_0- and ℓ_p-norm solutions of linear equalities, inequalities and linear programs for sufficiently small p," *J. Optim. Theory Appl.*, vol. 151, no. 1, pp. 1–10, 2011.

[30] V. Chandrasekaran, B. Recht, P. A. Parrilo, and A. S. Willsky, "The convex geometry of linear inverse problems," *Found. Comput. Math.*, vol. 12, no. 6, pp. 805–849, 2012.

[31] D. L. Donoho, "High-dimensional centrally symmetric polytopes with neighborliness proportional to dimension," *Discrete Comput. Geometry*, vol. 35, no. 4, pp. 617–652, 2006.

[32] D. L. Donoho and J. Tanner, "Precise undersampling theorems," *Proc. IEEE*, vol. 98, no. 6, pp. 913–924, Jun. 2010.

[33] D. L. Donoho, A. Maleki, and A. Montanari, "Message-passing algorithms for compressed sensing," *Proc. Nat. Acad. Sci. USA*, vol. 106, no. 45, pp. 18914–18919, 2009.

[34] J. F. C. Mota, N. Deligiannis, and M. Rodrigues, "Compressed sensing with side information: Geometrical interpretation and performance bounds," in *Proc. IEEE Global Conf. Signal Inf. Process., Symp. Inf. Process. Big Data*, 2014, pp. 512–516.

[35] J. F. C. Mota, L. Weizman, N. Deligiannis, Y. Eldar, and M. Rodrigues, "Reference-based compressed sensing: A sample complexity approach," in *Proc. IEEE Int. Conf. Acoust., Speech, Signal Process.*, 2016, pp. 4687–4691.

[36] J. F. C. Mota, N. Deligiannis, and M. R. D. Rodrigues, "Compressed sensing with prior information: Strategies, geometry, and bounds," *IEEE Trans. Inf. Theory*, vol. 63, no. 7, pp. 4472–4496, Jul. 2017.

[37] H. Van Luong, J. Seiler, A. Kaup, S. Forchhammer, and N. Deligiannis, "Measurement bounds for sparse signal reconstruction with multiple side information," arXiv:1605.03234.v2, 2016.

[38] E. J. Candès and Y. Plan, "A probabilistic and RIPless theory of compressed sensing," *IEEE Trans. Inf. Theory*, vol. 57, no. 11, pp. 7235–7254, Nov. 2011.

[39] M. Unser, "On the optimality of ideal filters for pyramid and wavelet signal approximation," *IEEE Trans. Signal Process.*, vol. 41, no. 12, pp. 3591–3596, Dec. 1993.

[40] M. Unser, "Ten good reasons for using spline wavelets," *Proc. SPIE*, vol. 3169, pp. 422–431, 1997.

[41] Y. Rivenson and A. Stern, "Compressed imaging with a separable sensing operator," *IEEE Signal Process. Lett.*, vol. 16, no. 6, pp. 449–452, Jun. 2009.

[42] B. Adcock, A. C. Hansen, C. Poon, and B. Roman, "Breaking the coherence barrier: A new theory for compressed sensing," *Forum of Mathematics, Sigma*, vol. 5, no. e4, 84 pp., 2017.

[43] A. Papoulis, *Signal Analysis*. New York, NY, USA: McGraw-Hill, 1977.

[44] H. Monajemi, J. Sina, M. Gavish, Stat 330/CME 362 Collaboration, and D. L. Donoho, "Deterministic matrices matching the compressed sensing phase transitions of gaussian random matrices," *Proc. Nat. Acad. Sci. USA*, vol. 110, no. 4, pp. 1181–1186, 2013.

[45] S. Mallat, *A Wavelet Tour of Signal Processing: The Sparse Way*, 3rd ed. New York, NY, USA: Academic, 2009.

[46] J. B. Buckheit and D. L. Donoho, "WaveLab and reproducible research," in *Wavelets and Statistics* (Lecture Notes in Statistics), vol. 103. New York, NY, USA: Springer, 1995, pp. 55–81.

[47] R. H. Tütüncü, K. C. Toh, and M. J. Todd, "Solving semidefinite-quadratic-linear programs using SDPT3," *Math. Program.*, vol. 95, no. 2, pp. 189–217, 2003.
[48] M. Grant and S. Boyd, "Graph implementations for nonsmooth convex programs," in *Recent Advances in Learning and Control* (Lecture Notes in Control and Information Sciences). New York, NY, USA: Springer-Verlag, 2008, pp. 95–110.
[49] M. Grant and S. Boyd, "CVX: Matlab software for disciplined convex programming," version 2.0 beta, Sep. 2013. [Online]. Available: http://cvxr.com/cvx
[50] D. L. Donoho, A. Maleki, and A. Montanari, "Supporting information to: Message passing algorithms for compressed sensing," 2009. [Online]. Available: http://www.stanford.edu/montanar/RESEARCH/FILEPAP/si.pdf
[51] P. Sen and S. Darabi, "A novel framework for imaging using compressed sensing," in *Proc. 2009 16th IEEE Int. Conf. Image Process.*, 2009, pp. 2133–2136.
[52] M. Stojnic, "Block-length dependent thresholds in block-sparse compressed sensing," arXiv:0907.3679, 2009.
[53] H. Yan, D. Blinder, S. Bettens, H. Ottevaere, A. Munteanu, and P. Schelkens, "CDF 9/7 wavelets as sparsifying operator in compressive holography," in *Proc. 2015 IEEE Int. Conf. Image Process.*, 2015, pp. 2015–2019.
[54] Y. Rivenson, A. Stern, and B. Javidi, "Overview of compressive sensing techniques applied in holography," *Appl. Opt.*, vol. 52, no. 1, pp. A423–432, 2013.
[55] Z. Yang, Z. Cishen, and X. Lihua, "On phase transition of compressed sensing in the complex domain," *IEEE Signal Process. Lett.*, vol. 19, no. 1, pp. 47–50, Jan. 2012.
[56] E. van den Berg and M. P. Friedlander, "Probing the Pareto frontier for basis pursuit solutions," *SIAM J. Sci. Comput.*, vol. 31, no. 2, pp. 890–912, 2008.
[57] E. van den Berg, "SPGL1: A solver for large-scale sparse reconstruction," 2007. [Online]. Available: http://www.cs.ubc.ca/labs/scl/spgl1.
[58] B. Adcock, A. C. Hansen, and R. Bogdan, "The quest for optimal sampling: Computationally efficient, structure-exploiting measurements for compressed sensing," in *Compressed Sensing and its Applications*. New York, NY, USA: Springer, 2015, pp. 143–167.

Stijn Bettens (S'16) received the M.Sc. degree in electronics and information technology engineering, in 2014, from Vrije Universiteit Brussel, Brussels, Belgium, where he is currently working toward the Ph.D. degree in the Department of Electronics and Informatics (ETRO). His research interests include regularization methods and compressive sensing for interference-based modalities, and digital holography in particular.

Colas Schretter (M'06) received the M.Sc. degree in computer science (with great Hons.) and an additional Master of Advanced Studies (DEA) degree from the Universite libre de Bruxelles, Brussels, Belgium, in 2004 and 2006, respectively. In February 2007, he moved to Germany for a scientist position with Philips Research, Aachen, Germany. Since October 2013, he has been a Senior Research Scientist in the ETRO Department, Vrije Universiteit Brussel, Brussels, Belgium. His research interests include problems in high-dimensional image formation using regularized inverse methods, statistical estimation for large mixture models, and quasi-Monte Carlo numerical integration. He received a Marie Curie EST Fellowship for his doctoral thesis, awarded with magna cum laude in April 2010, at Otto von Guericke University. Thereafter, he received a personal Marie Curie ERG Grant for a postdoctoral project with the RWTH Aachen University, and was a Visiting Researcher in the Politecnico di Milano, Milan, Italy. He was selected for a M+Vision 2012 Fellowship at the Massachusetts Institute of Technology, Cambridge, MA, USA.

Nikos Deligiannis (S'08–M'10) received the Diploma degree in electrical and computer engineering from the University of Patras, Patras, Greece, in 2006, and the Ph.D. degree (Hons.) in applied sciences from Vrije Universiteit Brussel, Brussels, Belgium, in 2012. He is currently an Assistant Professor in the Electronics and Informatics Department, Vrije Universiteit Brussel. From 2012 to 2013, he was a Postdoctoral Researcher with the Department of Electronics and Informatics, Vrije Universiteit Brussel. From 2013 to 2015, he was a Senior Researcher with the Department of Electronic and Electrical Engineering, University College London, London, U.K., and also a Technical Consultant on Big Visual Data Technologies with the British Academy of Film and Television Arts, U.K. His research interests include big data processing and analysis, machine learning, Internet-of-Things networks, and distributed signal processing. He has authored more than 80 journal and conference publications, book chapters, and two patent applications (one owned by iMinds, Belgium and the other by BAFTA, U.K.). He received the 2011 ACM/IEEE International Conference on Distributed Smart Cameras Best Paper Award, the 2013 Scientific Prize FWO-IBM Belgium, and the 2017 EURASIP Best Ph.D. Award.

Peter Schelkens (M'99) holds a professorship in the Department of Electronics and Informatics (ETRO), Vrije Universiteit Brussel, Brussels, Belgium, and is a Research Group Leader in the IMEC, Leuven, Belgium. His current research focuses on the multidimensional signal processing while especially focusing on cross-disciplinary research. In 2013, he received an EU ERC Consolidator Grant focusing on digital holography. He (co)authored more than 250 journal and conference publications and is the Coeditor of the books *The JPEG 2000 Suite* (Wiley, 2009) and *Optical and Digital Image Processing* (Wiley, 2011). He is an Associate Editor of the IEEE TRANSACTIONS ON CIRCUITS AND SYSTEMS FOR VIDEO TECHNOLOGY AND SIGNAL PROCESSING: IMAGE COMMUNICATIONS. He is a member of the ISO/IEC JTC1/SC29/WG1 (JPEG) standardization committee.